Synergistic role of Cu-C and Cu-N dual bonding of nanostructured g-C$_3$N$_4$/Cu$_2$SnS$_3$ photocatalysts for efficient CO$_2$ conversion to CO

Hossam A.E. Omr [a,b], Raghunath Putikam [c], Shien-Ping Feng [d], Ming-Chang Lin [c], Hyeonseok Lee [a,*]

[a] Department of Photonics, National Sun Yat-sen University, No. 70, Lien-Hai Rd, Kaohsiung 80424, Taiwan, ROC
[b] Department of Chemistry, Faculty of Science, Assiut University, Assiut 71516, Egypt
[c] Department of Applied Chemistry, National Yang-Ming Chiao Tung University, Hsinchu 300093, Taiwan, ROC
[d] Department of Advanced Design and Systems Engineering, City University of Hong Kong, Tat Chee Avenue, Hong Kong, SAR China

ARTICLE INFO

ABSTRACT

Herein, a 2D/0D g-C$_3$N$_4$/Cu$_2$SnS$_3$ heterostructure is successfully constructed via the facile calcination method, and its application to photocatalytic CO$_2$ conversion is demonstrated for the first time. The fabricated g-C$_3$N$_4$/Cu$_2$SnS$_3$ nanocomposite is featured with its unique Cu-C and Cu-N dual chemical bond at the interface. The engineered g-C$_3$N$_4$/Cu$_2$SnS$_3$ nanocomposites record a superior CO production rate of 18.2 μmol$\bullet$g^{-1}$\bullet$h^{-1} with an apparent quantum yield of 2.2% at 500 nm of light illumination, which is the highest among g-C$_3$N$_4$/ternary metal sulfide photocatalysts to the best of our knowledge. This notable improvement is attributed to the effective incorporation of Cu$_2$SnS$_3$ nanoparicles onto the surfaces of ultra-thin g-C$_3$N$_4$ and, the formation of Cu-N and Cu-C dual bonds at the interface. This helps not only the activation of interface defect-mediated Z-scheme conduction but also supplies highly reactive Cu sites in the Cu$_2$SnS$_3$ nanoparticles for efficient photocatalytic CO$_2$ conversion.

1. Introduction

For decades, enormous CO$_2$ emissions into the atmosphere from fossil fuel-dependent energy production to satisfy energy demand have become an essential reason for environmental issues such as climate change and global warming. Photocatalysis, as an attractive solution for these problems, has been suggested because it allows a photocatalyst to form useful fuels that require energy production, simultaneously removing CO$_2$ [1]. Since the monumental works by Halmann and Inoue et al. in 1978 and 1979, respectively, in this field [2,3], a huge number of semiconductor materials have been utilized for the photocatalytic conversion of CO$_2$ to fuels. In particular, inorganic semiconductors (TiO$_2$, WO$_3$, CdS, ZnO, ZnS, MoS$_2$, ZnIn$_2$S$_4$, etc.), organic semiconductors (conjugated microporous polymers and covalent organic frameworks), and hybrid materials (metal-organic frameworks and perovskites) have been demonstrated as photocatalysts for CO$_2$ conversion [4–8].

Two-dimensional (2D) graphitic carbon nitride (g-C$_3$N$_4$) has shown promising potential for photocatalytic CO$_2$ conversion among the materials listed above since the seminal work by Wang et al. in 2009 [9], due to its intriguing advantages: low toxicity, excellent CO$_2$ adsorption capability, high thermal and chemical stability, and its facile synthesis process from cheaper precursors. More importantly, the band structure of g-C$_3$N$_4$ is theoretically suitable to achieve the CO$_2$ reduction reaction (CO$_2$ RR) and water oxidation reaction that are required for CO$_2$ conversion. However, the insufficient light absorption property of g-C$_3$N$_4$ due to its wide optical bandgap results in limited CO$_2$ conversion. Moreover, numerous studies have clearly shown that incomplete polymerization of the precursors containing the amine group forms lots of hydrogen bonds in the g-C$_3$N$_4$ framework [10,11]. The hydrogen bonds become one of the main causes of decreased CO$_2$ conversion performance because they could induce detrimental factors such as inferior intralayer charge carrier transport and extensive photogenerated charge carrier recombination [10,11]. Thus, several strategies have been reported to overcome these limitations, including doping, copolymerization, and defect engineering [12,13]. In addition, the formation of ultra-thin 2D g-C$_3$N$_4$ nanosheets is of particular interest owing to their beneficial features, such as shortened carrier transport distance for

reaction, promoted separation of photogenerated electron-hole pairs, suppressed bulk recombination, and accessibility of interior atoms for surface defect engineering and interactions [14,15]. However, the enlarged band gap of ultra-thin g-C_3N_4 from the quantum confinement effect of its 2D structure further deteriorates the light absorption capability in the visible and infrared regions. Moreover, the naturally formed hydrogen bonds disturb intralayer charge transport more severely in the 2D g-C_3N_4 layer because of the potential energy barrier of 7.9 eV [10]. One of the interesting solutions to solve these problems is to break the hydrogen bonds [10,16]. The cleavage of the hydrogen bonds in ultra-thin g-C_3N_4 helps not only to overcome the potential barrier for promoted charge carrier dynamics but also to engineer optical properties to strengthen light absorption in the visible and near-infrared region by creating nitrogen vacancies [17,18]. For example, Li et al. proposed a B/P co-doping strategy to decrease the hydrogen bonds in the ultra-thin g-C_3N_4 structure, boosting the photocatalyst conversion efficiency [19]. Recently, ultra-thin g-C_3N_4 nanomesh with in-plane multi-holes and N defects exhibited outstanding visible light photocatalytic activity as a result of excellent physicochemical and charge carrier separation properties [20]. In 2023, Wu et al. utilized sulfuric acid to fabricate an S-doped ultra-thin g-C_3N_4 photocatalyst with low hydrogen bonds for a near-infrared light-driven H_2 evolution [21].

Further performance enhancement via photocatalysts, in general, is achievable by the incorporation of cocatalysts that can improve their properties by coupling with various metal or semiconductor materials [12,22,23]. In particular, metal sulfides could be one of the promising cocatalyst materials for further improved CO_2 conversion performance, forming a heterostructure with 2D ultra-thin g-C_3N_4 due to their widely extendable light absorption up to the visible (Vis) or even near infrared (NIR) region of light and the availability of more efficient charge carrier dynamics [24,25]. For instance, in 2016, Wang et al. reported the use of Sb_2S_3 to increase the photocatalytic activity by extending the light absorption of ultra-thin g-C_3N_4 nanosheet to the NIR region of the solar spectrum [25]. Chen et al. have also integrated $CdIn_2S_4$ with an ultra-thin g-C_3N_4 catalyst to maximize the catalyst performance by efficient visible light absorption [26]. Yang et al. fabricated ultra-thin ReS_2/g-C_3N_4 photocatalytic heterostructures to achieve a 2.7-fold improvement in H_2 evolution rate compared to that of pristine g-C_3N_4 through the optimization of the visible light capacity [27]. In addition, $ZnIn_2S_4$ was coupled with ultra-thin g-C_3N_4 to enhance the light absorption capacity, resulting in a 136.5-fold increase in the photocatalytic conversion efficiency compared to pure g-C_3N_4 [28].

In particular, the ternary metal sulfide Cu_2SnS_3 (CTS) is also of great interest because it possesses advantageous properties to form a successful heterojunction with 2D ultra-thin g-C_3N_4. CTS is basically suitable Vis-NIR light-harvesting material due to their small optical bandgap (0.8 – 1.7 eV) and showing p-type conduction. It is widely used in optical and photovoltaic devices due to its favorable properties, including material stability, nontoxicity, and high absorption coefficient ($\sim10^5\,cm^{-1}$) [29]. Furthermore, the uncoordinated metal sites in the diamond-like crystal structure of Cu_2SnS_3 nanoparticles (NPs) possibly suggest an interfacial chemical interaction with g-C_3N_4 [30,31]. Despite these valuable features, the investigation of CTS materials has been insufficient, and, to the best of our knowledge, no study has been implemented for photocatalytic CO_2 conversion with CTS materials [32–35].

In this work, ultra-thin g-C_3N_4 is successfully decorated with Cu_2SnS_3 NPs via the facile calcination method for the first demonstration of photocatalytic CO_2 conversion. The fabricated g-C_3N_4/Cu_2SnS_3 nanocomposites show a unique Cu-C and Cu-N dual bonds at the interface. The g-C_3N_4/Cu_2SnS_3 photocatalyst exhibits a superior CO production rate of 18.2 µmol•g^{-1}•h^{-1} with an apparent quantum yield of 2.2% at 500 nm, which is ~6 times higher than that of pristine g-C_3N_4. To the best of our knowledge, this superior performance is the highest among g-C_3N_4/ternary metal sulfide photocatalysts. The incorporation of Cu_2SnS_3 onto g-C_3N_4 not only boosts the visible-near infrared light energy harvest by its smaller bandgap but also reduces the

photogenerated charge carrier recombination. In addition, the formation of g-C_3N_4/Cu_2SnS_3 nanocomposite induces Z-scheme charge carrier conduction that is against the internal electrical field by its heterojunction. These extraordinary performances are enabled by the defects formed at the g-C_3N_4/Cu_2SnS_3 interface due to the formation of the Cu-N and Cu-C dual bonds, and more interestingly, Cu sites in the Cu-N and Cu-C dual bonds work as an essential component, providing highly activated reaction sites on CTS materials, which are studied in systematic experiments and simulations here.

2. Experimental section

2.1. Materials

Melamine (99%), Tin (II) chloride dihydrate ($SnCl_2$•2 H_2O, 98%), Potassium bicarbonate ($KHCO_3$, 99.7%, ACS reagent), Water-^{18}O ($H_2^{18}O$), and Triethanolamine (TEOA) were purchased from Sigma-Aldrich. Ammonium chloride (NH_4Cl, $\geq$99.5%) was bought from Honeywell/Fluka ™. Thiourea (NH_2CONH_2, +99%), lead (II) nitrate (Pb (NO_3), 99 + %), and copper (II) chloride pentahydrate ($CuCl_2$•5 H_2O, 99%, extra pure) were purchased from Acros Organics. 5,5-Dimethyl-1-pyrroline N-oxide (DMPO, 98%) was obtained from Matrix Scientific. Chloroplatinic acid hexahydrate (H_2PtCl_6•6 H_2O) was obtained from Alpha Aesar. Solvents, such as ethanol and ethylene glycol were of analytical grade.

2.2. Photocatalysts synthesis

2.2.1. Synthesis of ultra-thin g-C_3N_4 nanosheet

The ultra-thin g-C_3N_4 nanosheets (UCN) were prepared via the thermal treatment of melamine and NH_4Cl mixture [36]. In typical procedures, 5 g of melamine and 10 g of NH_4Cl are mixed in a ceramic crucible with a lid. The mixture was heated to 550 ℃ for 4 h with a heating rate of 2 ℃/min in a muffle furnace After cooling to room temperature, the product was collected and ground into a fine powder.

2.2.2. Synthesis of Cu_2SnS_3 nanoparticles

The synthesis of Cu_2SnS_3 was achieved by the hot-injection method, according to the literature [37]. Typically, 1.7 mmol of $CuCl_2$•5 H_2O and 0.8 mmol of $SnCl_2$•2 H_2O were dissolved in 50 mL of ethylene glycol in a 250-mL three-necked flask. The copper and tin precursors were purged with an inert gas for 30 min, heated to 100 ℃, and then heated to 190 ℃. At this temperature, the sulfur source (2.8 mmol of thiourea dissolved in 50 mL of ethylene glycol) was injected into the above metal precursors. The mixture was cooled down to room temperature and washed several times with deionized water and ethanol. The Cu_2SnS_3 nanoparticles (CTS NPs) were obtained by drying at 60 ℃ under a vacuum for 24 h.

2.2.3. Synthesis of 2D/0D g-C_3N_4/Cu_2SnS_3 heterostructured nanocomposites

The 2D/0D UCN/CTS heterostructures were delicately prepared through the facile calcination of the as-prepared UCN and CTS, as illustrated in Fig. 1a. Typically, 100 mg of g-C_3N_4 and a certain amount of Cu_2SnS_3 were ultrasonically dispersed in ethanol for 2 h. The mixture was vigorously stirred at 75 ℃ overnight. The obtained powder was dried at 85 ℃ for 12 h in a drying oven and subsequently calcined at 300 ℃ for 4 h in an Ar atmosphere. Following the same procedures, a series of g-C_3N_4/Cu_2SnS_3 nanocomposites, UCN/CTS-X, were prepared, in which X denotes a weight ratio of Cu_2SnS_3. UCN/CTS-Xs were synthesized with weight ratios of 1 wt%, 3 wt%, 5 wt%, and 7 wt% of Cu_2SnS_3, and the samples were named UCN/CTS-1, UCN/CTS-3, UCN/CTS-5, and UCN/CTS-7, respectively.

2.2.4. Preparation of physically mixed g-C_3N_4/Cu_2SnS_3

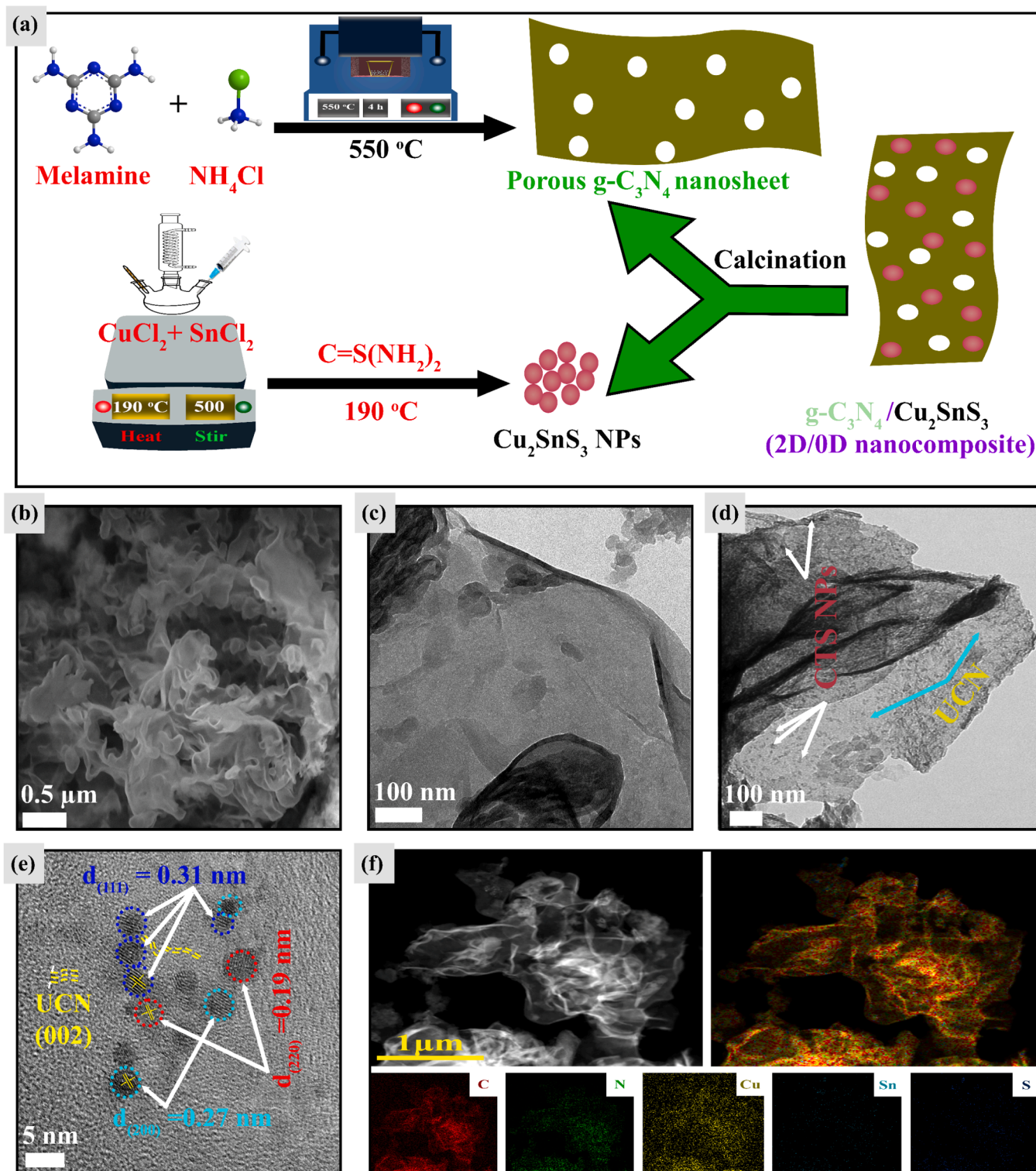The physically mixed composite was prepared by mixing the as-

Fig. 1. (a) Schematic illustration of 2D/0D UCN/CTS nanocomposite synthesis. (b) FE-SEM of UCN. TEM images of (c) UCN and (d) UCN/CTS-5. (e) HR-TEM and (f) HAADF-STEM images of UCN/CTS-5 nanocomposite.

prepared ultra-thin g-C_3N_4 nanosheet and Cu_2SnS_3 NPs. In detail, 100 mg of g-C_3N_4 were thoroughly ground with 5 wt% of Cu_2SnS_3 NPs in a mortar for 30 min and denoted as PM-UCN/CTS-5.

2.2.5. Synthesis of Pt NPs- decorated g-C_3N_4/Cu_2SnS_3

The photodeposition of Pt particles on the UCN/CTS-5 catalyst surface was carried out using H_2PtCl_6 as a precursor. 30 mg of UCN/CTS-5 was ultrasonically dispersed in 100 mL of 5 wt% Pt (H_2PtCl_6) aqueous solution containing 10 vol% of TEOA as a sacrificial agent, then the reaction mixture was purged by Ar gas for 30 min. The suspension was reacted under AM 1.5 illumination (100 mW/cm^2) for 2 h. Subsequently, the suspension was filtered, washed, and dried at 80 °C for 24 h. The obtained catalyst, denoted as Pt-UCN/CTS-5, was further analyzed.

2.2.6. Photodeposition of PbO_2 on g-C_3N_4/Cu_2SnS_3

The photodeposition of PbO_2 on the photocatalyst surface was achieved using $Pb(NO_3)$ as a precursor. Typically, 100 mg of $Pb(NO_3)$ was dissolved in 60 mL of deionized water by stirring for 30 min, then 20 mg of UCN/CTS-5 catalyst was added, and illuminated for 30 min. The obtained product was washed and dried overnight at 75 °C.

2.3. Photocatalytic CO_2 conversion by g-C_3N_4/Cu_2SnS_3 nanocomposites

The catalyst activity was tested in a stainless-steel reactor of 25 mL volume equipped with a quartz window. The reaction was performed under illumination of the solar simulator, equipped with a 100 W Xe lamp and an AM 1.5 filter. For the photocatalytic CO_2 conversion, the as-prepared photocatalyst powder was uniformly dispersed on a quartz disk and placed at the bottom of the reactor. Before the light irradiation, the reactor was evacuated three times by a mechanical pump. Subsequently, high-purity CO_2 (99.999%) was injected through a water bubbler into the reactor to make a CO_2/H_2O vapor mixture as described in Scheme S1. The gaseous products were quantified by gas chromatography (GC-2030 Nexis; SHIMADZU) equipped with a barrier discharge ionization detector (BID-2030). The apparent quantum yield (AQY) was investigated using band-pass monochromatic filters at wavelengths of 420, 460, and 500 nm, then calculated according to the previous report [38].

2.4. The electrochemical and photoelectrochemical measurements

The electrochemical measurements were performed using an electrochemical station (CHI-6081E) with a three-electrode system. The CO_2-saturated solution was prepared with 0.1 M $KHCO_3$ in DI water. The photocatalyst deposited on the FTO substrate was used as the working electrode. The Pt mesh and Ag/AgCl electrode were used as counter electrode and reference electrode, respectively. Electrochemical impedance spectroscopy (EIS) measurements were carried out under dark conditions and transient photocurrent (TPC) measurements were performed under AM 1.5 illumination (100 mW/cm^2). Details on the characterization and computational method of the catalysts are provided in the Supporting Information (Section S1).

3. Results and discussion

3.1. Preparation and characterization of 2D/0D g-C_3N_4/Cu_2SnS_3 heterostructure

The CTS material displayed nanoparticle morphology with an average diameter of $2 - 6$ nm, as shown in Fig. S1. In addition, the SAED pattern in Fig. S2 reveals that the synthesized CTS NPs have a polycrystalline nature with (111), (220), and (311) crystal planes. Fig. 1b and Fig. 1c show that the synthesized UCN sample forms the nanosheet morphology with a loose and soft texture as, in the work done by others [36,39]. The CTS NPs are homogenously distributed on the UCN surface without severe agglomeration as observed in Fig. 1d, suggesting the successful fabrication of 2D/0D UCN/CTS nanocomposites. Furthermore, the presence of diffraction patterns for CTS and UCN in the UCN/CTS-5 further confirms the delicate incorporation of CTS in the heterostructured catalyst with polycrystalline features (Fig. S3). In addition, the nanocomposite thickness of UCN/CTS-5 was recorded to be ~ 2.5 nm by AFM, and the corresponding height profile (Fig. S4) shows that the heterostructured catalyst has a length of a few hundred nanometers. Fig. 1e reveals that UCN/CTS-5 has lattice fringe spacings of around 0.31, 0.27, 0.19, and 0.32 nm that match the (111), (200), and (220) crystal planes of CTS material (JCPDS 89–2877) and (002) planes of UCN, respectively, further confirming the successful decoration of CTS onto the surface of UCN. Besides, the uniform distribution of the CTS NPs on the UCN surface is also observed from the HAADF-STEM image and corresponding EDX elemental maps of UCN/CTS-5 in Fig. 1f.

The N_2 adsorption-desorption isotherms for the UCN, CTS, and UCN/

CTS-5 samples were measured to assess the Brunauer-Emmet-Teller specific surface area (S_{BET}) and porosity structure (Fig. S5). The isotherm shape of all the samples belongs to type IV with an H3 hysteresis loop at a high relative pressure range ($0.8 -1.0$) that originated from the sheet stacking of the materials [40], indicating the dominated microporous structure of the as-synthesized catalysts as further proved from magnified TEM measurements (Fig. S6) [34,41]. The extracted S_{BET} for UCN is 103 m^2/g as in the reported works for UCN by others, and this is a more enlarged value than that from bulk g-C_3N_4 [42–44]. In comparison, the relatively modest S_{BET} reduction of the UCN/CTS-5 catalyst might be due to the partial blocking of UCN pores by loading CTS NPs during the synthesis of the heterostructured nanocomposites [45]. Additionally, the CO_2 adsorption capacity of the nanocomposite is improved compared to pristine UCN under the same pressure ($5.73 \rightarrow 6.41$ cm^3/g), as shown in Fig. S7.

To study the material and interface properties of the samples, XRD, FT-IR, and XPS measurements were conducted. Fig. 2a shows the XRD measurements of UCN, CTS, and UCN/CTS-X nanocomposites (X = 1, 3, 5, and 7 wt%). Two distinct diffraction peaks at $2\theta = 27.5$ ° and 12.7 ° are assigned to the (002) and (100) planes for the UCN catalyst as well as other g-C_3N_4-based materials [17,46–48]. These two peaks are attributed to van der Waals interlayer stacking and intralayer hydrogen bonds for maintaining the long-range structural order in g-C_3N_4 layers, respectively. For the cubic CTS crystal structure, there are six diffraction peaks at $2\theta = 28.4$ °, 32.9 °, 47.4 °, 56.2 °, 69.2 °, and 76.5 °, which are ascribed to (111), (200), (220), (311), (400), and (331) reflection planes, respectively (JCPDS 89–2877) [29]. The UCN/CTS-X samples show only the characteristic diffraction peaks from UCN without any CTS-related peaks that are already measured in Fig. 2a. This probably resulted from the low content and high dispersibility of CTS NPs on the UCN. The UCN/CTS-X samples show decreases in the two distinct diffraction peaks at $2\theta = 12.7$ ° and 27.5 ° of UCN as the CTS weight ratio increases in Fig. 2b and Fig. 2c, respectively. The decreased intensity at 12.7 ° suggests the loss of the ordered structure by the gradual breaking of intralayer hydrogen bonds of UCN in the nanocomposites after CTS decoration [17]. In addition, the slight 2θ shift from 27.5 ° in Fig. 2c, in comparison to pristine UCN, reveals the narrowed interlayer distance between the UCN layers in the composites. It is ascribed to the nitrogen vacancies created as a result of the strong π-π interaction between the layers [46]. Fig. 2d displays the FT-IR spectra of UCN and UCN/CTS-X nanocomposites. All samples exhibited a vibration peak located at 810 cm^{-1} that indexed to the out-of-plane breathing vibration of s-triazine units, while the detected vibrations (1200 -1700 cm^{-1}) are assigned to the skeletal stretching vibration of aromatic C_3N_4 heterocycle rings [47]. Additionally, the broad vibrational band centered at 3000–3300 cm^{-1} is assigned to N $-$ H stretching resulting from the incomplete condensation of amino groups on the surface of UCN. In comparison, the intensity of N $-$ H vibration in the composites decreased as shown in Fig. 2e, demonstrating the low terminal amino group contents of the UCN structure in the nanocomposites [11]. Moreover, the s-triazine peak (810 cm^{-1}) of the nanocomposites shifts to a higher wavenumber in Fig. 2f, implying a stronger vibration and movement of the electron cloud of C$-$N and C$=$N bonds in the UCN framework as a result of the chemical bonding at the interface [48]. Also, Raman spectroscopy was recorded to further confirm the incorporation of CTS NPs in the nanocomposite. Fig. S8 reveals the presence of Raman bands for CTS and UCN in the nanocomposite [49,50]. Interestingly, two new bonds at Raman shifts of about 170 cm^{-1} and 430 cm^{-1} for Cu$-$C and Cu$-$N bonds are introduced in the UCN/CTS-5, respectively, as shown in Fig. S8 [51,52].

Further elemental and bonding properties of the samples were investigated with XPS as shown in Fig. 3. With the survey spectra in Fig. S9, all elements (i.e., C, N, Cu, Sn, and S) were detected from the nanostructured UCN/CTS-5 catalyst, which is in good agreement with the elemental mapping results in Fig. 1f. Fig. 3a presents the high-resolution C 1 s spectra of UCN and UCN/CTS-5 catalysts. For the
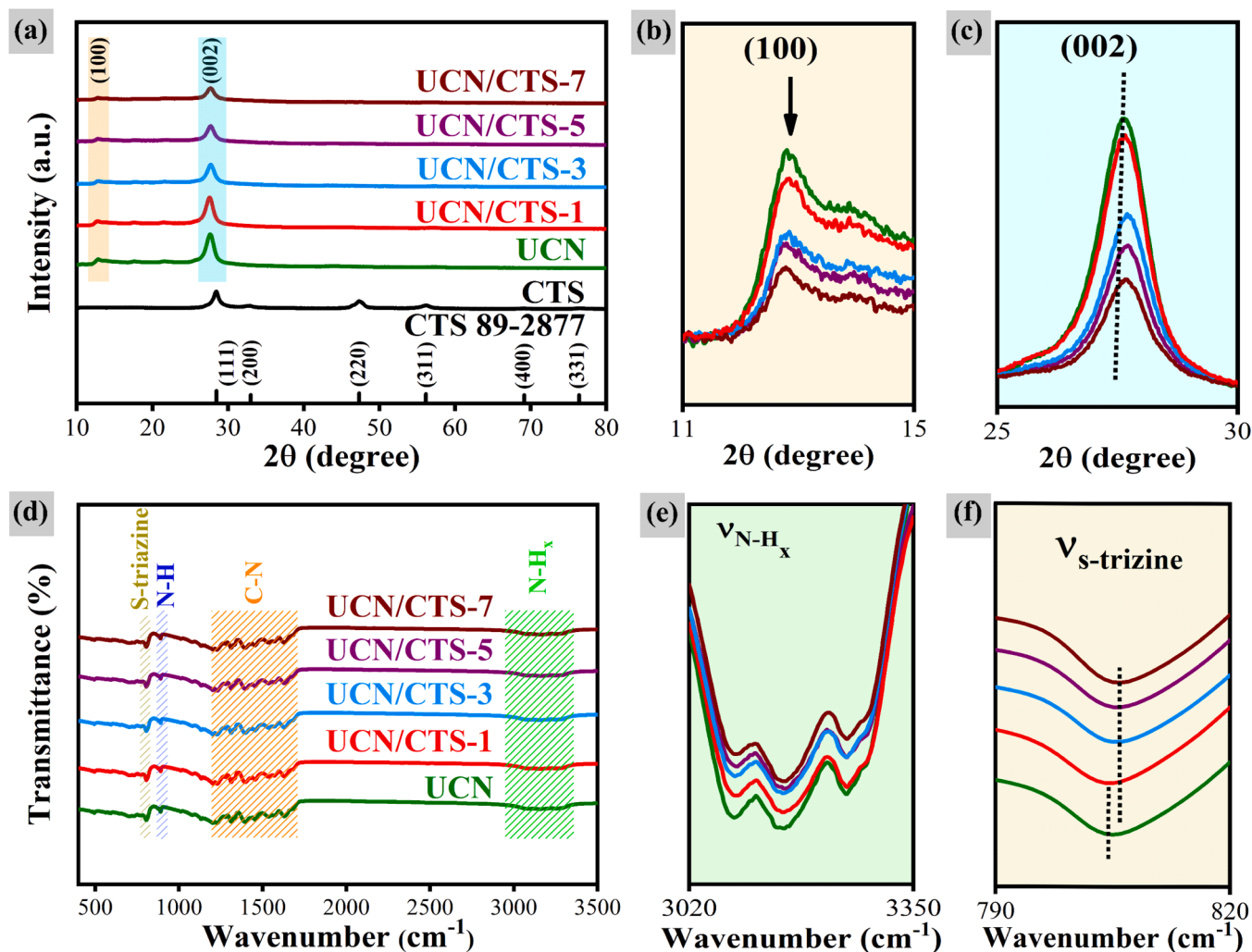
Fig. 2. (a) XRD patterns of UCN, CTS, and UCN/CTS-X nanocomposites. Enlarged XRD patterns at 2θ range of (b)11 ° − 15 ° and (c) 25 ° − 30 ° for UCN and UCN/CTS-X. (d) FT-IR spectra of UCN and UCN decorated with different CTS content. Enlarged FT-IR spectrum at wavenumber range of (e) 3020−3350 cm^{-1} and (f) 790−820 cm^{-1} for UCN and UCN/CTS-X.

UCN sample, the four peaks centered at 284.5 eV, 285.7 eV, 287.8 eV, and 289.0 eV were attributed to sp^2 C–C bonds, C−NH$_x$, C(−N)$_3$, and sp^2-bonded carbon N − C═N, respectively [39,53]. For UCN/CTS-5, the additional peak at 282.6 eV could be attributed to the Cu−C bond formation, as in the previous report [54]. Fig. 3b illustrates the N 1 s spectra of UCN and UCN/CTS-5 nanocomposite. Three distinct peaks located at 398.4 eV, 399.8 eV, and 401.0 eV are observed and indexed for sp^2-bonded nitrogen C−N = C, tertiary nitrogen groups N(−C)$_3$, and C−NH$_x$, respectively [39,53]. These three peaks are denoted as N$_a$, N$_b$, and N$_c$, respectively, for more analysis. In addition, a new peak at 397.4 eV is observed for the UCN/CTS-5 catalyst, which is ascribed to the formation of Cu−N bond at the interface between UCN and CTS in the nanocomposite [55]. This Cu-N bond makes a dual chemical bond together with the Cu-C bond in Fig. 3a in our sample, suggesting uniquely novel and strong dual coupling among g-C$_3$N$_4$-based composites as listed in Table S1. Moreover, HR-XPS spectra of C 1 s and N 1 s (Fig. S10) for the physically mixed composite (i.e., PM-UCN/CTS-5) show the disappearance of the assigned peaks for Cu-C and Cu-N bonds, further confirming the uniquely introduced dual bonds originated from our fabrication processes of UCN /CTS heterostructure. Moreover, it is worth noting that there is a positive shift in the core electron binding energy for C 1 s and N 1 s of the UCN/CTS-5 catalyst, evidencing the successful formation of a heterojunction through dual chemical bonding [25]. The interaction of CTS with UCN displayed a

decrease in the concentration of nitrogen in N$_c$ sites, demonstrating the partial loss of amino groups in the nanostructured catalyst and resulting in the partial breaking of interlayered hydrogen bonds in the UCN framework. Moreover, the area ratio between C−N = C and N(−C)$_3$ peaks, namely, N$_a$/N$_b$, as provided in Table S2, is reduced to 2.69 compared to that of UCN (2.77). This suggests the presence of a nitrogen vacancy in the C−N = C structure [56]. These observations are also consistent with the results from XRD and FT-IR measurements, revealing that the incorporation of CTS NPs onto UCN can cause the formation of nitrogen vacancies in C−N = C sites and the gradual loss of the terminal amino group in the g-C$_3$N$_4$ framework simultaneously. In Fig. 3c, the Cu 2p spectra of CTS materials possess two distinct peaks located at 932.8 eV and 952.7 eV, corresponding to Cu 2p$_{3/2}$ and Cu 2p$_{1/2}$, respectively. The peaks at 487.8 eV and 495.7 eV in the Sn 3d XPS spectra of CTS (Fig. 3d) correspond to Sn 3d$_{5/2}$ and Sn 3d$_{3/2}$, respectively. In Fig. 3e, the high-resolution S 2p spectrum identifies two peaks at 161.9 eV and 163.1 eV that are assigned to 2p$_{3/2}$ and 2p$_{1/2}$ of CTS, respectively [35]. The negative shifts in the binding energies of Cu 2p, Sn 3d, and S 2p in the UCN/CTS-5 catalyst (Fig. 3c-e), further prove the effective pn heterojunction via the dual chemical bond between CTS and UCN.

The defective structure of UCN was further investigated by room-temperature electron paramagnetic resonance (EPR) measurements in Fig. 3f. It is reported that the single Lorentzian line of unpaired electrons
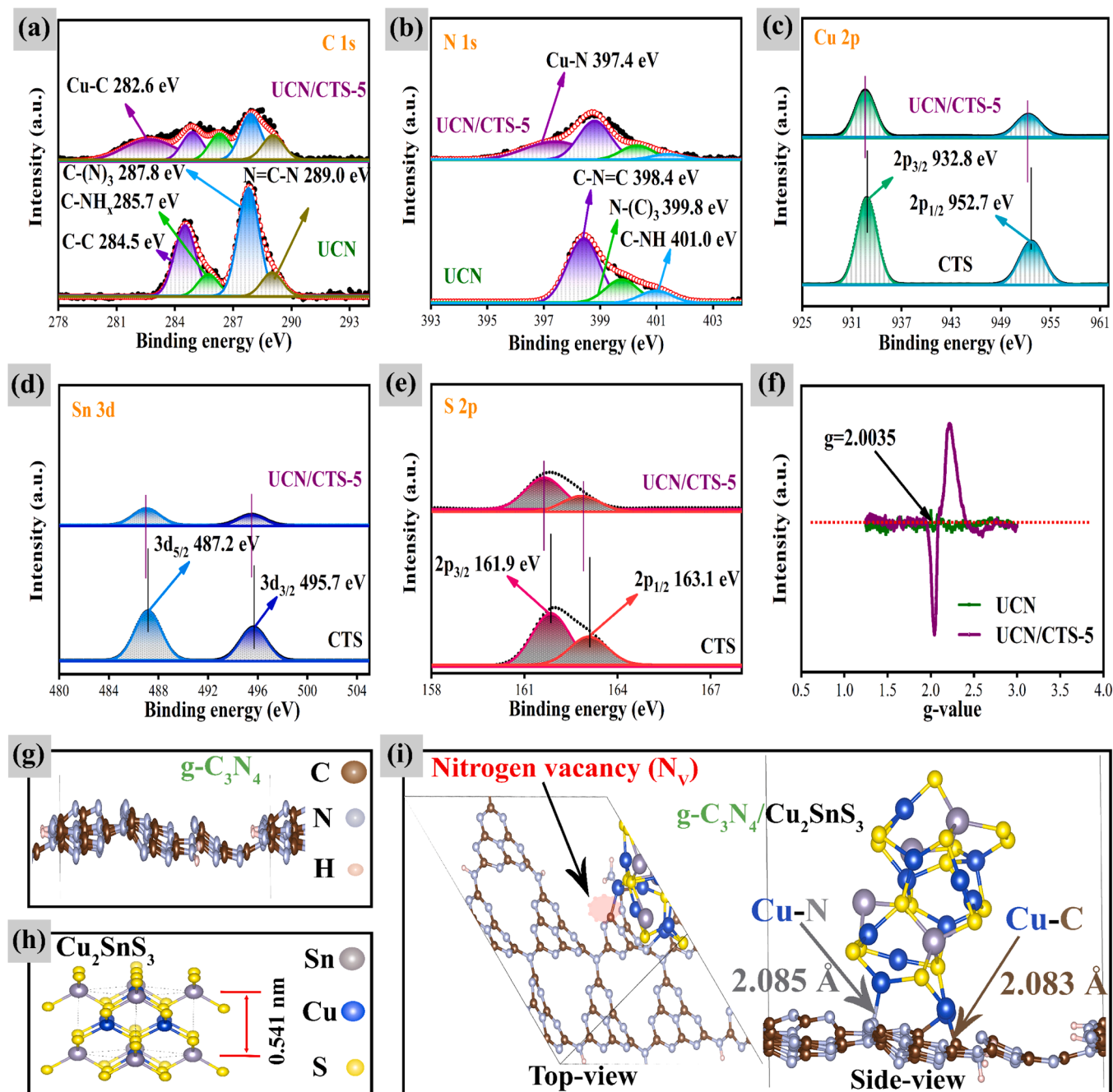
Fig. 3. HR-XPS spectra of C 1 s (a) and N 1 s (b) for UCN and UCN/CTS-5 catalysts. HR-XPS spectra of Cu 2p (c), Sn 3d (d), and S 2p (e) for CTS and UCN/CTS-5. (f) EPR spectra of UCN and UCN/CTS-5 catalysts. Simulated structural models for (g) g-C$_3$N$_4$, (h) Cu$_2$SnS$_3$, and (i) g-C$_3$N$_4$/Cu$_2$SnS$_3$ heterostructure.

for the sp^2 carbon atom on UCN is 2.0035 [56]. Thus, the enhanced EPR signal of the UCN/CTS-5 catalyst suggests a high concentration of delocalized electrons and can be interpreted as the presence of nitrogen defects [11]. Moreover, the g-value deviation from the free electron value might be associated with the spin-orbit coupling effect that results from the chemically bonded UCN with copper in the heterostructured catalyst [57]. To further comprehend the structural properties of our fabricated heterostructure, Fig. 3g-i depict the simulated g-C$_3$N$_4$, Cu$_2$SnS$_3$, and g-C$_3$N$_4$/Cu$_2$SnS$_3$ models. The g-C$_3$N$_4$ framework consisted of amino-rich heptazine moieties, as depicted in Fig. 3g [58]. Fig. 3h demonstrates that the Cu$_2$SnS$_3$ is crystallized in the cubic space group P-43 m (a= 0.541 nm), which is consistent with the reported results (a = 0.543 nm) [32]. Intriguingly, the model of the heterostructured catalyst (Fig. 3i) is simulated with the presence of nitrogen vacancies (N$_V$)

together with Cu−C and Cu−N dual bonds with lengths of 2.083 and 2.085 Å, respectively, corresponding to the XRD, EPR, and XPS findings. Moreover, the interface bond energy of g-C$_3$N$_4$/Cu$_2$SnS$_3$ was calculated to be − 2.09 eV, proving the highly stable interface of the heterostructured catalyst because of the interfacial dual bonds.

3.2. Photocatalytic CO$_2$ conversion performance of heterostructured 2D/0D g-C$_3$N$_4$/Cu$_2$SnS$_3$ catalysts

The CO$_2$ conversion efficiency of our heterostructured photocatalysts was tested under AM 1.5 illumination at ambient conditions. As displayed in Fig. 4a, pristine UCN produces 3.0 μmol•g^{-1}•h^{-1} of CO. After coupling with CTS, the heterostructured photocatalysts (i.e., UCN/CTS-X) show improved photocatalytic CO$_2$ conversion performance. With the
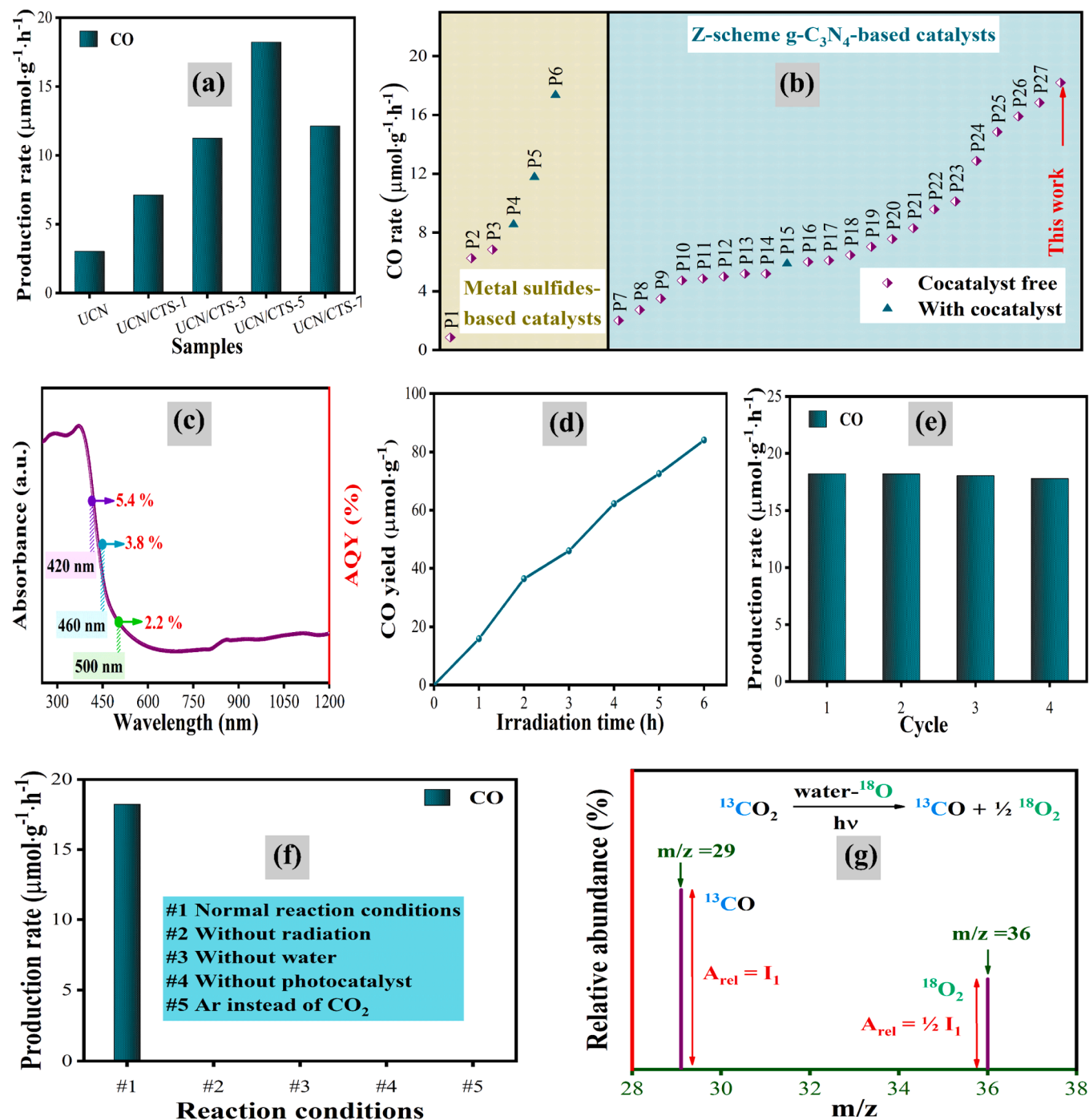
Fig. 4. (a) CO production rates for UCN and UCN/CTS-X photocatalysts, (b) comparison of CO production rates among g-C_3N_4-based heterostructured photocatalysts (the abbreviated catalysts are provided in Tables S3, S4, and S5), (c) action spectrum of CO evolution by UCN/CTS-5 catalyst. (d) the CO production yield of UCN/CTS-5 as a function of irradiation time, (e) recyclability experiment of UCN/CTS-5 through 2-hour photocatalytic CO_2 conversion, (f) CO production rates of UCN/CTS-5 under various reaction conditions, and (g) GC-Mass analysis using $^{13}CO_2$ and $H_2^{18}O$ for photocatalytic CO_2 conversion by UCN/CTS-5 catalyst (A_{rel} refers to relative abundance).

increasing weight ratio of the CTS, the CO generation rate gradually increased, while the excessive CTS content reduced the photocatalyst conversion efficiency. Among the fabricated UCN/CTS-X catalysts, UCN/CTS-5 exhibits the highest CO production rate of 18.2 $\mu mol \bullet g^{-1} \bullet h^{-1}$, which is around 6 times higher than that of UCN. The action spectrum of CO_2-to-CO conversion by UCN/CTS-5 was conducted at different wavelengths, as shown in Fig. 4c. Obviously, the apparent quantum yield (AQY) of CO production was 2.2% at 500 nm and reached 5.4% at 420 nm, suggesting the light-induced CO_2-to-CO

conversion process. To the best of our knowledge, 18.2 $\mu mol \bullet g^{-1} \bullet h^{-1}$ of the CO production rate by UCN/CTS-5 is the highest among g-C_3N_4/ ternary metal sulfides, g-C_3N_4/quaternary metal sulfides, and heterostructured g-C_3N_4 photocatalysts with and without cocatalysts, as shown in Fig. 4b and listed in Tables S3, S4, and S5, respectively. Moreover, with increasing illumination time, the UCN/CTS-5 photocatalyst exhibits a linear increase in CO yield, and the accumulated CO yield is 84.1 $\mu mol \bullet g^{-1}$ for 6 h, as shown in Fig. 4d, proving the long-term stable CO_2 conversion by our photocatalysts together with the excellent

recyclability as shown in Fig. 4e. In addition, the XRD, FT-IR, TEM, HR-TEM, and HADDF-STEM measurements display no significant change in crystallinity, chemical bonding, morphological structure, or elemental composition after the cycling experiment, demonstrating the excellent material stability of our photocatalyst as shown in Figs. S11, S12, and S13. We believe that the structural stability of the catalyst could be attributed to the unique dual bond at the interface.

The conducted control experiments under different reaction conditions in Fig. 4f indicate that the produced CO gas originates from the photocatalytic CO_2 conversion by the UCN/CTS photocatalysts. The origin of CO is additionally evidenced by the isotope tracer $^{13}CO_2$ experiment in Fig. 4g. Moreover, the H_2O oxidation to O_2 was detected by the water-^{18}O labeling experiment, as shown in Fig. 4g. Herein, the signals at $m/z = 29$ and $m/z = 36$ are assigned to ^{13}CO and $^{18}O_2$ with a ratio of 2: 1, respectively, suggesting the mass balance according to equation (1).

$$^{13}CO_2 \xrightarrow{hv, water-^{18}O} {}^{13}CO + 1/2\, ^{18}O_2 \qquad (1)$$
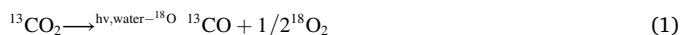
3.3. Optical properties of g-C₃N₄/Cu₂SnS₃ photocatalysts

The optical properties of the fabricated catalysts were characterized via ultraviolet-visible-near-infrared diffuse reflectance spectroscopy (UV-Vis-NIR DRS) in Fig. 5a. The UCN catalyst has limited visible light harvesting ability, which stems from its wider band gap of 2.9 eV (Fig. S14) owing to the quantum confinement effect of ultra-thin g-C₃N₄ [59]. However, with the incorporation of the CTS NPs, UCN/CTS-Xs exhibit remarkable absorbance enhancement both in the Vis and NIR regions, and the enhancement becomes stronger with the higher contents of the CTS NPs. The boosted Vis-NIR light absorption capacity of UCN/CTS-X photocatalysts in Fig. 5a could be attributed to two reasons: (1) the uniquely excellent Vis-NIR harvesting ability of the CTS NPs that originates from its small bandgap of 1.59 eV [60] as shown in Fig. S15 and Fig. S16, and the right inset of Fig. 5a; and (2) visible light absorption by newly created energy states in the optical bandgap of the UCN material due to the presence of nitrogen vacancies and partial cleavage of hydrogen bonding [17] as discussed in Fig. 2, Fig. 3 and Table S2, together with the widespread Urbach tail near band edges confirmed in Fig. S17 [61,62]. Nevertheless, the excessive CTS content (i.e., UCN/CTS-7) is not helpful for light absorption enhancement, probably owing to the severe aggregation of CTS NPs on the UCN surface as in Fig. S18. These results coincide with the CO_2 conversion experiment in Fig. 4a.

3.4. Charge carrier dynamic characterizations

The study on the dynamics of photogenerated electron-hole pairs for heterostructured UCN/CTS-X was conducted using room-temperature photoluminescence (RT-PL) spectra and time-resolved photoluminescence (TR-PL) spectra in Fig. 5b and Fig. 5c. As demonstrated by previous research, the significant emission peak at 400–550 nm in Fig. 5b is related to the band-to-band recombination of photogenerated electron-hole pairs in UCN [17]. However, the PL emission is strongly quenched with the incorporation of CTS NPs from all the UCN/CTS-X samples in spite of the presence of the unfavorable internal electric field in its pn heterojunction identified in Fig. 3, demonstrating greatly suppressed radiative recombination. This can be explained by the presence of localized energy states by nitrogen vacancies at the
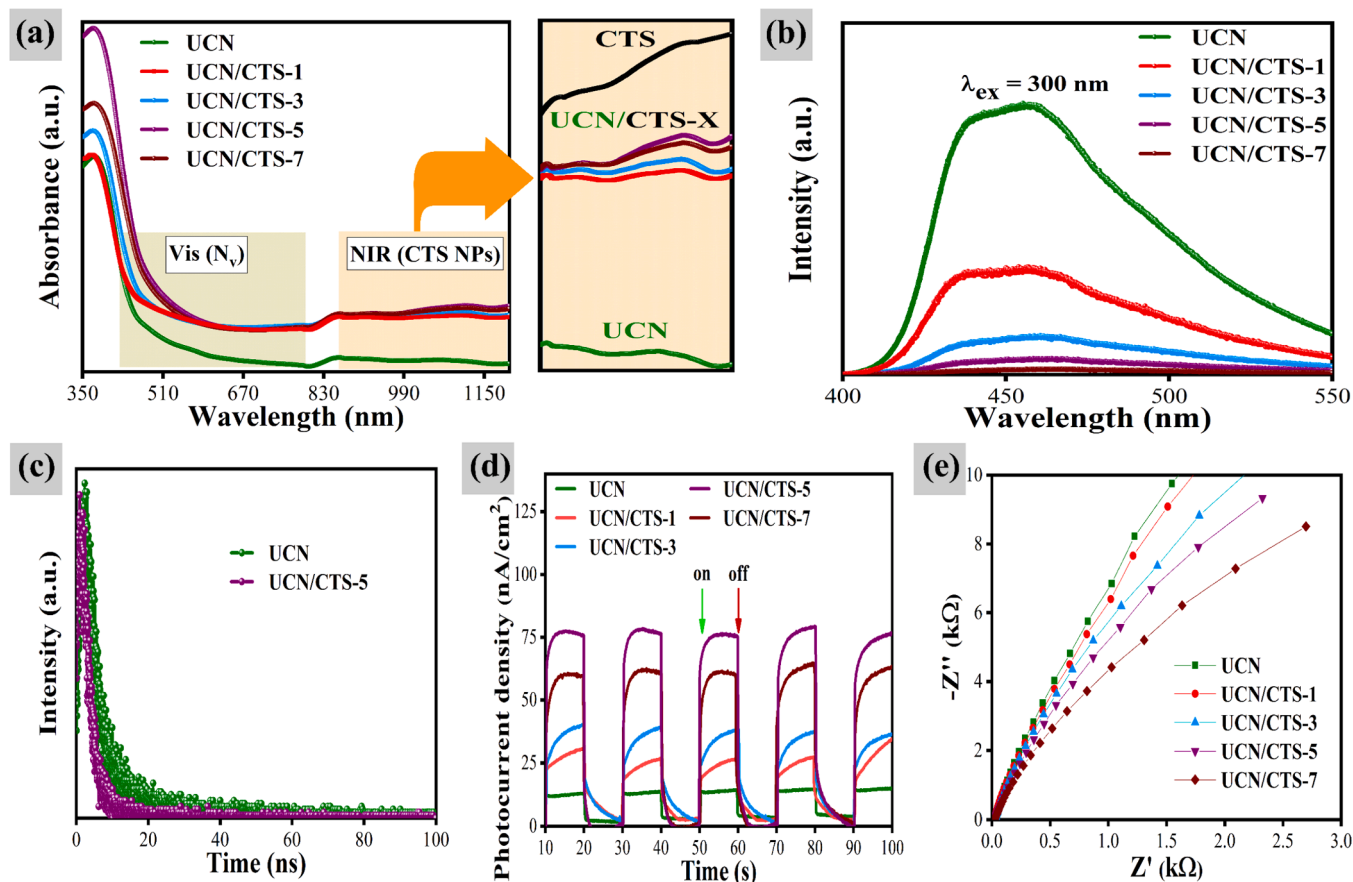
Fig. 5. (a) UV-Vis-NIR DRS of UCN and UCN/CTS-X (the right inset is the enlarged NIR region of UCN, CTS, and UCN/CTS-X). (b) RT-PL spectra of UCN and UCN/CTS-X catalysts at the 300 nm excitation wavelength. (c) TR-PL spectroscopy of UCN and UCN/CTS-5 catalysts. TPC measurements (d) and EIS spectra (e) of UCN and UCN/CTS-X samples in CO_2-saturated 0.1 M KHCO₃ solution at 0.4 V of applied bias.

UCN/CTS interface, which enables dual bond-bridged Z-scheme charge transfer mediated by the localized energy states at the UCN/CTS interface, as in other reports [7].

Further analysis was implemented with the TR-PL measurement in Fig. 5c. The extracted carrier lifetime of the UCN/CTS-5 is shorter (τ_{avg} = 1.46 ns) than that of the pristine UCN (τ_{avg} = 3.48 ns). This means that charge carrier transport is improved from UCN to CTS owing to the presence of localized states at the UCN/CTS interface [63] and also suggests excellent carrier separation and transfer toward CTS via the localized defects at the UCN/CTS interface. This efficient charge transfer dynamics could benefit the accumulation of the photogenerated electrons and holes on CTS and UCN, respectively, which is an essential factor for highly efficient CO_2 conversion.

Further experiments were additionally performed to examine photocurrent response and electron migration impedance in a CO_2-saturated electrolyte using transient photocurrent (TPC) and electrochemical impedance spectroscopy (EIS) techniques, as shown in Fig. 5d and Fig. 5e. All the UCN/CTS-Xs show improved photoresponses, and UCN/CTS-5 displays the highest photocurrent density among catalysts in Fig. 5d, revealing that the enhanced Vis-NIR light absorption in Fig. 5a generates more photogenerated charge carriers on the catalyst

surface, which is directly helpful for efficient CO_2 production, as shown in Fig. 4. The Nyquist plot from the EIS measurement (Fig. 5e) exhibits a larger charge transfer resistance at the UCN/CO_2 interface (i.e., a larger semicircle diameter of the Nyquist plot). However, this charge transfer resistance was reduced by CTS decoration, indicating efficient charge transfer at the photocatalyst/CO_2 interface with higher adsorption affinity of CO_2 molecules on the heterostructured catalyst surface, as shown in Fig. S6. Furthermore, the dual bonds-based heterostructured photocatalyst shows significantly reduced charge transfer resistance at the photocatalyst/CO_2 interface (Fig. S19) compared to the catalyst without interfacial bonds.

3.5. Mechanistic study of photocatalytic CO_2 conversion by g-C_3N_4/Cu_2SnS_3 heterostructures.

For the analysis of the band structure, the valence band XPS (VB-XPS) spectra were conducted to show that the valence band edges (E_{VB}) of our fabricated UCN and CTS NPs are 2.25 eV and 0.25 eV, respectively, in Fig. S20. The measured values of E_{VB} are also equivalent to 2.18 V and 0.18 V ($E_{VB, NHE}$) for UCN and CTS, respectively. Following the formula ($E_{CB, NHE} = E_{VB, NHE} - E_g$), the calculated conduction band
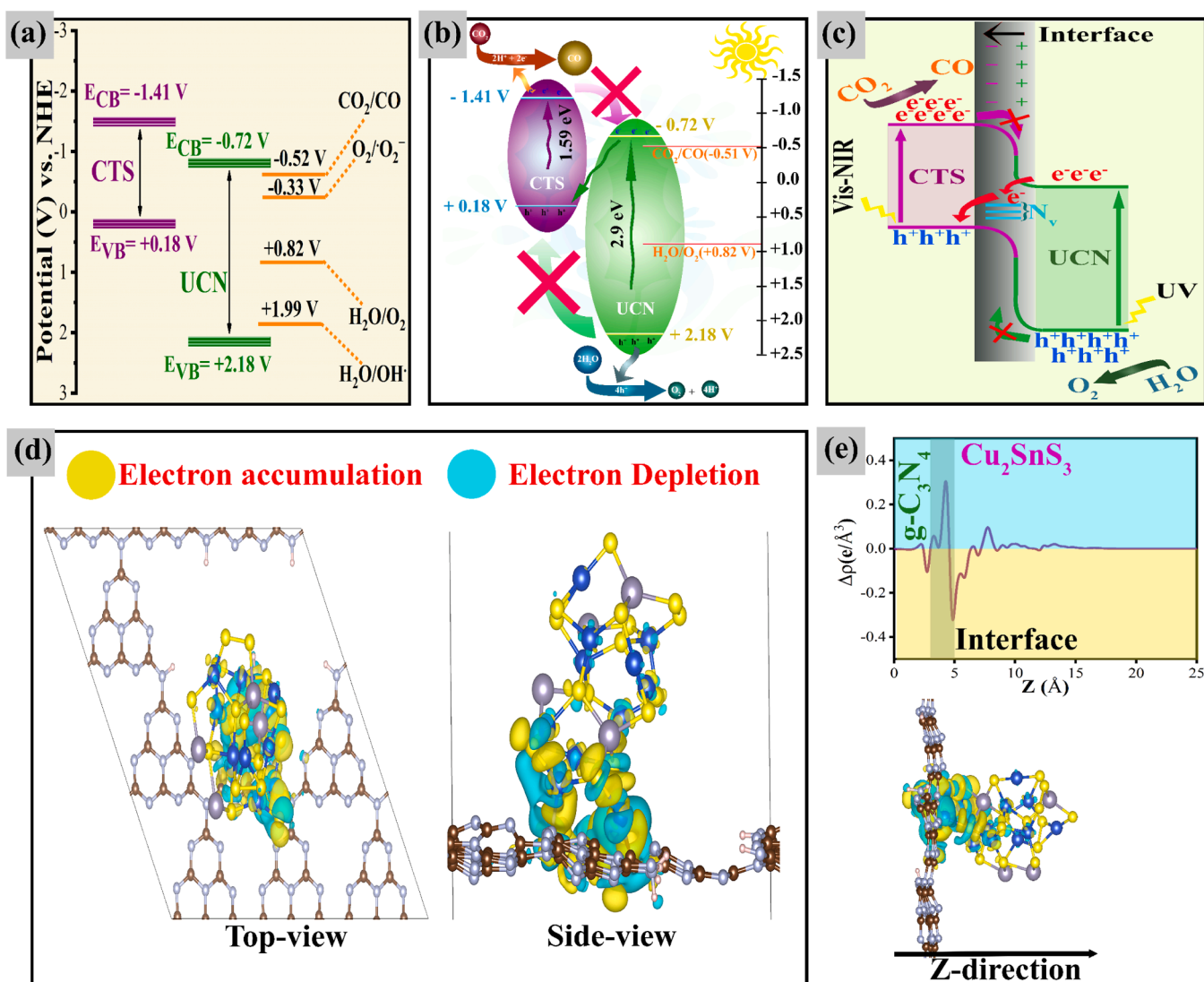
Fig. 6. Schematic band diagram energy of UCN and CTS (a) before and (b) after heterostructured junction construction. (c) proposed surface defects-mediated Z-scheme charge transfer mechanism of the UCN/CTS-5 catalyst. (d) Top- and side-views of simulated charge density difference for UCN/CTS heterostructured catalyst. (e) the calculated planar-averaged charge density distribution for the UCN/CTS.

edges ($E_{CB, NHE}$) of UCN and CTS are − 0.72 and − 1.41 V, respectively.

Based on VB-XPS results and Tauc plots, the band energy diagrams of pure UCN and CTS can be described as shown in Fig. 6a. Our fabricated 2D/0D g-C_3N_4/Cu_2SnS_3 catalyst has a staggered gap configuration due to the $E_{VB, NHE}$ position of CTS near the $E_{CB, NHE}$ of UCN. From a thermodynamic standpoint, the photocatalytic CO_2 RR can be achieved on the pure UCN and CTS materials because of the theoretical potentials of CO_2/CO (− 0.52 V vs NHE), while the water oxidation is only preferred on the surface of pure UCN due to the H_2O/O_2 potential level (+ 0.82 V vs. NHE) as shown in Fig. 6a. After the formation of the pn heterojunction in Fig. 6b, the photogenerated electrons move to the VB of CTS, annihilating holes in the VB through Z-scheme carrier conduction, which helps to accumulate electrons and holes for CTS and UCN, respectively. Accordingly, the Cu_2SnS_3 NPs and g-C_3N_4 in the nanocomposite act as reductive and oxidative catalysts for CO_2 reduction and water oxidation, respectively. This Z-scheme carrier conduction is beneficial for more vibrant CO_2 conversion because a larger energy difference between E_{CB} and CO_2 reduction potential can strengthen the driving force of electrons, improving the CO_2 conversion rate [64]. In other words, the electron accumulation on CTS can accelerate the CO_2 RR. In our sample, despite the presence of an unfavorable internal electric field, the Z-scheme carrier conduction is highly activated due to the interfacial defect states (N_V) via the Cu−C and Cu−N bonding for vibrant CO_2 RR on the conduction band (CB) of CTS and water oxidation on the VB of UCN, as depicted in Fig. 6c.

This charge distribution by the UCN and CTS band structures is further confirmed with DFT simulation in Figs. 6d and 6e. The DFT results visualize the electron accumulation on the CTS surface in the UCN/CTS catalyst, forming pn junctions at the UCN/CTS interface through the Cu−C and Cu−N bonding together with the interface defects. Interestingly, it is found that the electrons are more concentrated around Cu−C and Cu−N dual bonds in Fig. 6d. Additionally, even in the DFT simulation, the electrons and holes distribution at the UCN/CTS interface is obviously demonstrated, corresponding with the simulated work functions of UCN (5.27 eV) and CTS (5.70 eV) in Fig. S21. All these results show that the Cu−C and Cu−N dual bonds play an important role in charge transport and, thereby, CO_2 conversion performance in the UCN/CTS catalyst. Even in the experiment with a physical mixture of UCN/CTS-5 composite, the importance of the dual bond was remarkable. Our fabricated composites exhibit remarkable emission quenching compared to the physically mixed composite in Fig. S22, suggesting that the dual bonds are a key factor for excellent charge transfer. In addition, the severely deteriorated CO_2 conversion performances with the pristine UCN and physically mixed nanocomposite in Fig. 4a and Fig. S23, respectively, also exhibit the essential role of the dual bond for efficient CO_2 conversion. Also, the dual bonds-based heterostructured catalyst has enhanced CO_2 adsorption compared to that of without interfacial bonds as shown in Fig. S24.

To examine the redox capability of our samples and further prove the charge carrier transfer mechanism, DMPO spin trapping electron paramagnetic resonance (EPR) spectra for UCN, CTS, and UCN/CTS-5 are measured in Figs. 7a and 7b. Fig. 7a demonstrates that the photogenerated electrons in CTS CB have the greatest reduction ability due to the strongest EPR signal of CTS compared to UCN due to the more negative potential of $E_{CB, NHE}$ than the potential of $O_2/{}^\bullet O_2^-$ (−0.33 V, NHE) [41] as shown in Fig. 6a. On the contrary, ${}^\bullet OH$ can only be produced on the UCN surface in Fig. 7b owing to the more positive E_{VB} position than the potential of $H_2O/OH\bullet$ (+1.99 V, NHE) as shown in Fig. 6a [41]. Thus, the photogenerated holes in UCN VB have the strongest oxidative ability than that of pure CTS. However, it is worth noting that the heterostructured UCN/CTS-5 catalyst generated higher DMPO-${}^\bullet O_2^-$ and DMPO-${}^\bullet OH$ adducts than other samples. Thereby, the heterostructured catalyst exhibits the highest levels of reductive and oxidative ability for the generation of ${}^\bullet O_2^-$ and ${}^\bullet OH$ as a result of the remarkable accumulation of photogenerated electrons and holes on the CTS CB and UCN VB, respectively. These results can demonstrate the

activation of interfacial defects-mediated Z-scheme pathway via dual chemical bonds. To experimentally visualize the carrier transfer pathway of our samples, the photodeposition of Pt and PbO_2 particles on the UCN/CTS-5 catalyst surface were implemented in Fig. S25. The HR-TEM image in Fig. S25a reveals that Pt NPs preferentially deposit near CTS NPs in the UCN/CTS-5 catalyst. Also, the PbO_2 NPs were photo-deposited on the surface of UCN, and far from the CTS NPs in Fig. S25b. Accordingly, the photogenerated electrons and holes are respectively accumulated more on the CTS and UCN surfaces because of the efficient electron transfer through the dual bond channels at the interface. This finding is also congruent with the suggested dual chemical bonds-bridged Z-scheme transfer mechanism through the interfacial defects.

The CO_2-to-CO conversion process by our UCN/CTS catalyst is further investigated by DFT simulation for understanding CO formation. The widely accepted CO_2-to-CO reduction pathway by a photocatalyst is shown in Eqs. (2)–(5) below [65].

$$* + CO_{2(g)} \rightarrow CO_2^* \tag{2}$$

$$CO_2^* + H^+ + e^- \rightarrow COOH^* \tag{3}$$

$$COOH^* + H^+ + e^- \rightarrow CO^* + H_2O \tag{4}$$

$$CO^* \rightarrow CO_{(g)} + * \tag{5}$$

where * is a catalytically active site. For further insight into the highly improved CO_2-to-CO conversion by UCN/CTS photocatalyst, the Gibbs free energy (ΔG) diagram for the essential species was simulated and depicted in Fig. 7 based on the equations above. Firstly, DFT simulations were conducted to identify the atomistic catalytic sites for CO_2 reduction and H_2O oxidation by the UCN/CTS catalyst. Evidently, the water adsorption is more thermodynamically favorable on the N sites of g-C_3N_4 in the nanocomposite, as shown in Fig. S26. On the other hand, the overall free energy for the CO_2-to-CO reduction pathway (Fig. 7c) on the Cu site is − 0.74 eV, while the Sn and S sites are 0.42 eV and − 0.34 eV, respectively, suggesting that Cu or S sites are thermodynamically favorable sites for CO_2 reduction. However, the most negative overall free energy ($\Delta G_{overall} = −0.74$ eV) imply that the CO_2 conversion reaction occurs mainly via Cu sites that make effective dual bonds with C and N elements in UCN. In addition, the CO_2 molecules are more strongly adsorbed on the Cu sites than on the S sites, as shown by the high isosurface value (Fig. 7d) and this probably contributes to the enhancement of CO_2 adsorption in Fig. S7. The enhanced CO_2 adsorption could be also ascribed to strong electron exchange between the electron-rich Cu site and the antibonding orbital of CO_2 [66]. This results from the high density of states (DOS) by Cu atoms compared to S atoms as shown in Fig. S27. Moreover, the weekly interaction of CO species with the Cu sites demonstrated by the low isosurface value in Fig. 7e, facilitating the desorption of CO from the catalyst surface. This Cu site in UCN/CTS catalyst exhibits − 0.20 eV of lowered free energy for CO_2^* formation, $\Delta G_{CO_2^*}$, in comparison to that of the pristine catalyst ($\Delta G_{ads} = −0.08$ eV) as shown in Fig. 7f, suggesting its stronger CO_2 affinity toward the surface. This is more helpful for obtaining a high capacity of CO_2 uptake, which is one of the crucial prerequisites for a highly efficient CO_2 conversion [65]. In addition, the free energy of CO_2^* on the surface of g-C_3N_4 is positively shifted after the formation of the UCN/CTS heterostructure, as shown in Fig. 7f and Fig. S28 (−0.08 eV → −0.06 eV). This positive shift in the free energy of CO_2^* proves the CO_2 reduction and water oxidation reactions occur on separated semiconductors as explained in Fig. 6. The formation of COOH* species during the photocatalytic reaction is the rate-limiting step for CO_2 conversion [65] and its formation energy barrier with the UCN/CTS heterostructured catalyst shows − 0.51 eV of the lowered value, while UCN has relatively unfavorable formation energy of 0.9 eV. This more negative exothermicity with UCN/CTS indicates the strong binding of
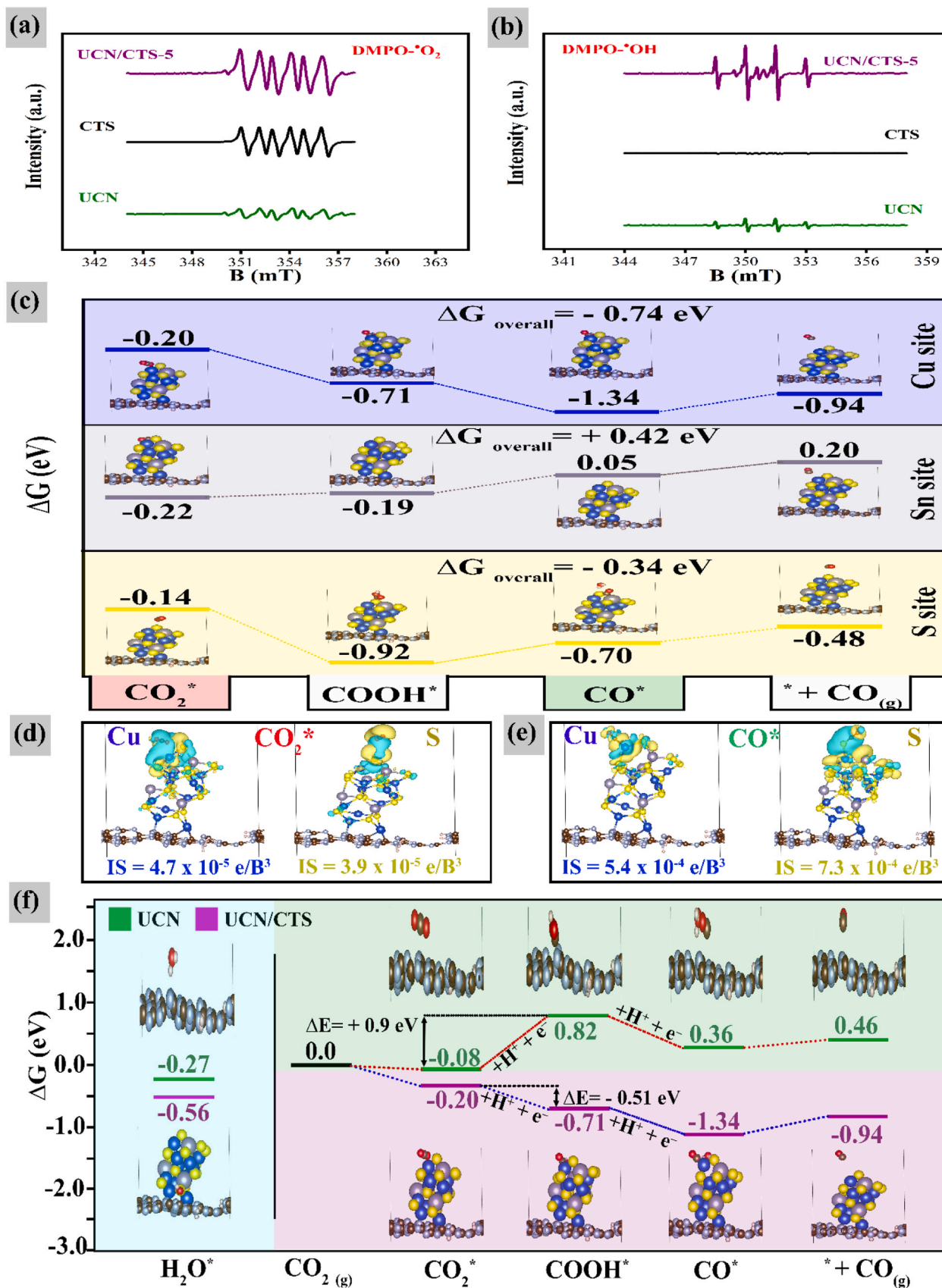
Fig. 7. EPR spectra for UCN, CTS, and UCN/CTS-5 catalysts of (a) DMPO-$^{\bullet}O_2^{-}$ adducts and (b) DMPO-$^{\bullet}OH$ adducts under light illumination. (c) simulated free energy models for CO_2-to-CO conversion for UCN/CTS photocatalyst at different catalytic active sites. Simulated charge density difference and isosurface values (IS) for (d) CO_2 and (e) CO species adsorbed on Cu and S sites of the g-C_3N_4/Cu_2SnS_3 catalyst. (f) calculated free energy models for the UCN and Cu sites of UCN/CTS catalysts.

the intermediate specie, COOH* , with the catalyst surface, which is thermodynamically favorable in efficient photocatalysis [67]. Furthermore, the heterostructured photocatalyst exhibited higher water adsorption energy than UCN, as displayed in Fig. 7f. All these DFT simulation results demonstrate that the CO_2 conversion by our UCN/CTS heterostructured photocatalysts can be highly activated by effective Cu sites through Cu-C and Cu-N dual bonds.

4. Conclusion

In summary, interface defect-mediated Z-scheme 2D/0D UCN/CTS heterostructured photocatalysts have been successfully synthesized via a facile calcination method for CO_2 conversion applications. The CTS NPs are tightly bound to the UCN framework via dual Cu-N and Cu-C bonds. The UCN /CTS photocatalyst exhibits a superior CO production rate of 18.2 $\mu mol \bullet g^{-1} \bullet h^{-1}$ with an apparent quantum yield of 2.2% at 500 nm, which is about 6 times higher than that of pristine g-C_3N_4. This superior performance, to the best of our knowledge, is the highest among g-C_3N_4/ ternary metal sulfide photocatalysts. This promoted performance could be attributed to the formation of the Cu-C and Cu-N dual bonds at the UCN/CTS interface. The benefits from the dual bonds for the UCN/CTS photocatalysts are as follows: (1) the promoted CO_2 adsorption capacity on UCN/CTS-X nanocomposite with highly activated Cu sites in Cu_2SnS_3 NPs; (2) the improved Vis-NIR light absorption via the induced nitrogen vacancies by breaking of intralayer hydrogen bonds, and the excellent optical properties of CTS NPs; (3) the spatial separation of reduction and oxidation active sites to maximize the redox abilities; (4) the suppressed radiative recombination and efficient transport & separation of photo-generated charge carriers via the Cu-C and Cu-N dual chemical bonds bridged Z-scheme mediated by interface defects; (5) outstanding structural and interface stability of the photocatalyst. This work visualizes the potential of new composite materials for the photocatalytic CO_2 conversion field and offers a novel design and profound knowledge for a dual chemical bond-modulated Z-scheme heterojunction for further development.

CRediT authorship contribution statement

H. A. E. Omr: Conceptualization, Visualization, Investigation, Methodology, Formal analysis, Data curation, Writing – original draft. **R. Putikam:** Investigation, Methodology, Data curation, Writing – review & editing. **S.P Feng:** Investigation, Writing – review & editing. **M. C. Lin:** Investigation, Writing – review & editing. **H. Lee:** Conceptualization, Investigation, Data curation, Writing – review & editing, Supervision, Funding acquisition, Project administration, Validation, Resources.

Declaration of Competing Interest

The authors declare that they have no known competing financial interests or personal relationships that could have appeared to influence the work reported in this paper.

Data Availability

Data will be made available on request.

Appendix A. Supporting information

Supplementary data associated with this article can be found in the online version at doi:10.1016/j.apcatb.2023.123103.

References

[1] J. Ran, M. Jaroniec, S.Z. Qiao, Cocatalysts in semiconductor-based photocatalytic CO_2 reduction: achievements, challenges, and opportunities, Adv. Mater. 30 (2018) 1704649.

[2] M. Halmann, Photoelectrochemical reduction of aqueous carbon dioxide on p-type gallium phosphide in liquid junction solar cells, Nature 275 (1978) 115–116.

[3] T. Inoue, A. Fujishima, S. Konishi, K. Honda, Photoelectrocatalytic reduction of carbon dioxide in aqueous suspensions of semiconductor powders, Nature 277 (1979) 637–638.

[4] M. Liras, M. Barawi, A. Víctor, Hybrid materials based on conjugated polymers and inorganic semiconductors as photocatalysts: from environmental to energy applications, Chem. Soc. Rev. 48 (2019) 5454–5487.

[5] D. Voiry, H.S. Shin, K.P. Loh, M. Chhowalla, Low-dimensional catalysts for hydrogen evolution and CO_2 reduction, Nat. Rev. Chem. 2 (2018) 1–17.

[6] R.R. Ikreedeegh, M. Tahir, A critical review in recent developments of metal-organic-frameworks (MOFs) with band engineering alteration for photocatalytic CO2 reduction to solar fuels, J. CO2 Util. 43 (2021), 101381.

[7] X. Li, C. Garlisi, Q. Guan, S. Anwer, K. Al-Ali, G. Palmisano, L. Zheng, A review of material aspects in developing direct Z-scheme photocatalysts, Mater. Today 47 (2021) 75–107.

[8] Y.W. Teh, C.-M. Fung, M.K. Chee, J. Low, S.-T. Yong, S.-P. Chai, Broadening cognizance on atomically thin photocatalysts, Mater. Today 43 (2021) 198–212.

[9] X. Wang, K. Maeda, A. Thomas, K. Takanabe, G. Xin, J.M. Carlsson, K. Domen, M. Antonietti, A metal-free polymeric photocatalyst for hydrogen production from water under visible light, Nat. Mater. 8 (2009) 76–80.

[10] C. Yang, S. Zhang, Y. Huang, K. Lv, S. Fang, X. Wu, Q. Li, J. Fan, Sharply increasing the visible photoreactivity of g-C_3N_4 by breaking the intralayered hydrogen bonds, Appl. Surf. Sci. 505 (2020), 144654.

[11] D. Zhao, C.L. Dong, B. Wang, C. Chen, Y.C. Huang, Z. Diao, S. Li, L. Guo, S. Shen, Synergy of dopants and defects in graphitic carbon nitride with exceptionally modulated band structures for efficient photocatalytic oxygen evolution, Adv. Mater. 31 (2019) 1903545.

[12] Q. Xu, Z. Xia, J. Zhang, Z. Wei, Q. Guo, H. Jin, H. Tang, S. Li, X. Pan, Z. Su, Recent advances in solar-driven CO_2 reduction over g-C_3N_4-based photocatalysts, Carbon Energy, (2022).

[13] M.K. Hussien, A. Sabbah, M. Qorbani, M.H. Elsayed, S. Quadir, P. Raghunath, D.-L. M. Tzou, S.-C. Haw, H.-H. Chou, N.Q. Thang, Numerous defects induced by exfoliation of boron-doped g-C_3N_4 towards active sites modulation for highly efficient solar-to-fuel conversion, Materials Today, Sustainability 22 (2023), 100359.

[14] M. Aggarwal, S. Basu, N.P. Shetti, M.N. Nadagouda, E.E. Kwon, Y.-K. Park, T. M. Aminabhavi, Photocatalytic carbon dioxide reduction: Exploring the role of ultrathin 2D graphitic carbon nitride (g-C_3N_4), Chem. Eng. J. 425 (2021), 131402.

[15] D. Chen, Y. Zou, S. Wang, Surface chemical-functionalization of ultrathin two-dimensional nanomaterials for electrocatalysis, Materials Today, Energy 12 (2019) 250–268.

[16] J. Meng, X. Wang, Y. Liu, M. Ren, X. Zhang, X. Ding, Y. Guo, Y. Yang, Acid-induced molecule self-assembly synthesis of Z-scheme WO_3/g-C_3N_4 heterojunctions for robust photocatalysis against phenolic pollutants, Chem. Eng. J. 403 (2021), 126354.

[17] Y. Kang, Y. Yang, L.C. Yin, X. Kang, L. Wang, G. Liu, H.M. Cheng, Selective breaking of hydrogen bonds of layered carbon nitride for visible light photocatalysis, Adv. Mater. 28 (2016) 6471–6477.

[18] Y. Li, M. Yang, Y. Xing, X. Liu, Y. Yang, X. Wang, S. Song, Preparation of carbon-rich g-C_3N_4 nanosheets with enhanced visible light utilization for efficient photocatalytic hydrogen production, Small 13 (2017) 1701552.

[19] B. Li, Y. Si, B.-X. Zhou, Q. Fang, Y.-Y. Li, W.-Q. Huang, W. Hu, A. Pan, X. Fan, G.-F. Huang, Doping-induced hydrogen-bond engineering in polymeric carbon nitride to significantly boost the photocatalytic H_2 evolution performance, ACS Appl. Mater. Interfaces 11 (2019) 17341–17349.

[20] C. Hao, J. Zhang, N. Li, T. Zhou, E. Xiaoye, X. Zhao, Size-dependent design of ultrathin g-C_3N_4 nanomesh with N defects towards superior visible-light photocatalytic efficiency, Colloids Surf, A Physicochem Eng. Asp. 649 (2022), 129534.

[21] X. Wu, D. Li, B. Luo, B. Chen, Y. Huang, T. Yu, N. Shen, L. Li, W. Shi, Molecular-level insights on NIR-driven photocatalytic H_2 generation with ultrathin porous S-doped g-C_3N_4 nanosheets, Appl. Catal. B 325 (2023), 122292.

[22] H.A. Omr, M.W. Horn, H. Lee, Low-dimensional nanostructured photocatalysts for efficient CO_2 conversion into solar fuels, Catalysts 11 (2021) 418.

[23] H.A. Omr, R. Putikam, M.K. Hussien, A. Sabbah, T.-Y. Lin, K.-H. Chen, H.-L. Wu, S.-P. Feng, M.-C. Lin, H. Lee, Design of sculptured SnS/g-C3N4 photocatalytic nanostructure for highly efficient and selective CO2 conversion to methane, Appl. Catal. B (2022), 122231.

[24] J. Wang, S. Lin, N. Tian, T. Ma, Y. Zhang, H. Huang, Nanostructured metal sulfides: classification, modification strategy, and solar-driven CO_2 reduction application, Adv. Funct. Mater. 31 (2021) 2008008.

[25] H. Wang, X. Yuan, H. Wang, X. Chen, Z. Wu, L. Jiang, W. Xiong, G. Zeng, Facile synthesis of Sb_2S_3/ultrathin g-C_3N_4 sheets heterostructures embedded with g-C_3N_4 quantum dots with enhanced NIR-light photocatalytic performance, Appl. Catal. B 193 (2016) 36–46.

[26] W. Chen, T. Huang, Y.-X. Hua, T.-Y. Liu, X.-H. Liu, S.-M. Chen, Hierarchical $CdIn_2S_4$ microspheres wrapped by mesoporous g-C_3N_4 ultrathin nanosheets with

enhanced visible light driven photocatalytic reduction activity, J. Hazard. Mater. 320 (2016) 529–538.

[27] T. Yang, Y. Shao, J. Hu, J. Qu, X. Yang, F. Yang, C.M. Li, Ultrathin layered 2D/2D heterojunction of ReS$_2$/high-crystalline g-C$_3$N$_4$ for significantly improved photocatalytic hydrogen evolution, Chem. Eng. J. (2022), 137613.

[28] X. Dang, M. Xie, F. Dai, J. Guo, J. Liu, X. Lu, Ultrathin 2D/2D ZnIn$_2$S$_4$/g-C$_3$N$_4$ nanosheet heterojunction with atomic-level intimate interface for photocatalytic hydrogen evolution under visible light, Adv. Mater. Interfaces 8 (2021) 2100151.

[29] S.B. Jathar, S.R. Rondiya, Y.A. Jadhav, D.S. Nilegave, R.W. Cross, S.V. Barma, M. P. Nasane, S.A. Gaware, B.R. Bade, S.R. Jadkar, Ternary Cu$_2$SnS$_3$: synthesis, structure, photoelectrochemical activity, and heterojunction band offset and alignment, Chem. Mater. 33 (2021) 1983–1993.

[30] A. Lokhande, S. Pawar, E. Jo, M. He, A. Shelke, C. Lokhande, J.H. Kim, Amines free environmentally friendly rapid synthesis of Cu$_2$SnS$_3$ nanoparticles, Opt. Mater. 58 (2016) 268–278.

[31] Y. Shen, C. Li, R. Huang, R. Tian, Y. Ye, L. Pan, K. Koumoto, R. Zhang, C. Wan, Y. Wang, Eco-friendly p-type Cu$_2$SnS$_3$ thermoelectric material: crystal structure and transport properties, Sci. Rep. 6 (2016) 1–8.

[32] V.R.M. Reddy, M.R. Pallavolu, P.R. Guddeti, S. Gedi, K.K.Y.B. Reddy, B. Pejjai, W. K. Kim, T.R.R. Kotte, C. Park, Review on Cu$_2$SnS$_3$, Cu$_3$SnS$_4$, and Cu$_4$SnS$_4$ thin films and their photovoltaic performance, J. Ind. Eng. Chem. 76 (2019) 39–74.

[33] S. Yao, L. Xu, Q. Gao, X. Wang, N. Kong, W. Li, J. Wang, G. Li, X. Pu, Enhanced photocatalytic degradation of Rhodamine B by reduced graphene oxides wrapped-Cu2SnS3 flower-like architectures, J. Alloy. Compd. 704 (2017) 469–477.

[34] M.B. Zaman, R. Poolla, Morphological tuning of hydrothermally derived visible light active Cu$_2$SnS$_3$ nanostructures and their applications in photocatalytic degradation of reactive industrial dyes, Opt. Mater. 104 (2020) 109853.

[35] J. Xu, R. Wang, X. Chen, R. Zhou, J. Zhang, Cu$_2$SnS$_3$ nanocrystals decorated rGO nanosheets towards efficient and stable hydrogen evolution reaction in both acid and alkaline solutions, Materials Today, Energy 17 (2020) 100435.

[36] X. Lu, K. Xu, P. Chen, K. Jia, S. Liu, C. Wu, Facile one step method realizing scalable production of gC3N4 nanosheets and study of their photocatalytic H2 evolution activity, J. Mater. Chem. A 2 (2014) 18924–18928.

[37] U.V. Ghorpade, M.P. Suryawanshi, S.W. Shin, I. Kim, S.K. Ahn, J.H. Yun, C. Jeong, S.S. Kolekar, J.H. Kim, Colloidal wurtzite Cu$_2$SnS$_3$ (CTS) nanocrystals and their applications in solar cells, Chem. Mater. 28 (2016) 3308–3317.

[38] S. Sorcar, Y. Hwang, C.A. Grimes, S.-I. In, Highly enhanced and stable activity of defect-induced titania nanoparticles for solar light-driven CO2 reduction into CH4, Mater. Today 20 (2017) 507–515.

[39] M.K. Hussien, A. Sabbah, M. Qorbani, M.H. Elsayed, P. Raghunath, T.-Y. Lin, S. Quadir, H.-Y. Wang, H.-L. Wu, D.-L.M. Tzou, Metal-free four-in-one modification of g-C$_3$N$_4$ for superior photocatalytic CO$_2$ reduction and H$_2$ evolution, Chem. Eng. J. 430 (2022), 132853.

[40] X. Zhao, D. Han, M. Dai, Y. Fan, Z. Wang, D. Han, L. Niu, Direct Z-scheme FeV$_2$O$_4$/g-C$_3$N$_4$ binary catalyst for highly selective reduction of carbon dioxide, Chem. Eng. J. 436 (2022), 132051.

[41] H. Guo, S. Wan, Y. Wang, W. Ma, Q. Zhong, J. Ding, Enhanced photocatalytic CO$_2$ reduction over direct Z-scheme NiTiO$_3$/g-C$_3$N$_4$ nanocomposite promoted by efficient interfacial charge transfer, Chem. Eng. J. 412 (2021), 128646.

[42] C. Zhang, J. Liu, X. Huang, D. Chen, S. Xu, Multistage polymerization design for g-C$_3$N$_4$ nanosheets with enhanced photocatalytic activity by modifying the polymerization process of melamine, ACS Omega 4 (2019) 17148–17159.

[43] S. Yan, Z. Li, Z. Zou, Photodegradation performance of g-C$_3$N$_4$ fabricated by directly heating melamine, Langmuir 25 (2009) 10397–10401.

[44] P. Xia, B. Zhu, J. Yu, S. Cao, M. Jaroniec, Ultra-thin nanosheet assemblies of graphitic carbon nitride for enhanced photocatalytic CO2 reduction, J. Mater. Chem. A 5 (2017) 3230–3238.

[45] D. Zeng, W. Xu, W.-J. Ong, J. Xu, H. Ren, Y. Chen, H. Zheng, D.-L. Peng, Toward noble-metal-free visible-light-driven photocatalytic hydrogen evolution: monodisperse sub–15 nm Ni$_2$P nanoparticles anchored on porous g-C$_3$N$_4$ nanosheets to engineer 0D–2D heterojunction interfaces, Appl. Catal. B 221 (2018) 47–55.

[46] X. Hao, J. Zhou, Z. Cui, Y. Wang, Y. Wang, Z. Zou, Zn-vacancy mediated electron-hole separation in ZnS/g-C$_3$N$_4$ heterojunction for efficient visible-light photocatalytic hydrogen production, Appl. Catal. B 229 (2018) 41–51.

[47] Y. Xu, X. Jin, T. Ge, H. Xie, R. Sun, F. Su, X. Li, L. Ye, Realizing efficient CO$_2$ photoreduction in Bi$_3$O$_4$Cl: constructing van der Waals heterostructure with g-C$_3$N$_4$, Chem. Eng. J. 409 (2021), 128178.

[48] J. Feng, D. Zhang, H. Zhou, M. Pi, X. Wang, S. Chen, Coupling P nanostructures with P-doped g-C$_3$N$_4$ as efficient visible light photocatalysts for H$_2$ evolution and RhB degradation, ACS Sustain. Chem. Eng. 6 (2018) 6342–6349.

[49] M. Belaqziz, K. Medjnoun, K. Djessas, H. Chehouani, S. Grillo, Structural and optical characterizations of Cu$_2$SnS$_3$ (CTS) nanoparticles synthesized by one-step green hydrothermal route, Mater. Res. Bull. 99 (2018) 182–188.

[50] X. Bai, L. Wang, Y. Wang, W. Yao, Y. Zhu, Enhanced oxidation ability of g-C$_3$N$_4$ photocatalyst via C$_{60}$ modification, Appl. Catal. B 152 (2014) 262–270.

[51] T. Bruhm, A. Abram, J. Häusler, O. Thomys, K. Köhler, Walter reppe revival–identification and genesis of copper acetylides Cu$_2$C$_2$ as active species in ethynylation reactions, Chem. Eur. J. 27 (2021) 16834–16839.

[52] K. Mavridou, M. Zervos, F. Pinakidou, M. Brzhezinskaya, M. Katsikini, Oxidation of Cu$_3$N thin films obtained from Cu annealed under NH$_3$: O$_2$ flow: A Raman and NK-edge NEXAFS, Study, J. Alloy. Compd. 914 (2022), 165293.

[53] L. Shi, L. Liang, J. Ma, F. Wang, J. Sun, Enhanced photocatalytic activity over the Ag$_2$O–g-C$_3$N$_4$ composite under visible light, Catal. Sci. Technol. 4 (2014) 758–765.

[54] D.O. Adekoya, M. Tahir, N.A.S. Amin, g-C$_3$N$_4$/(Cu/TiO$_2$) nanocomposite for enhanced photoreduction of CO$_2$ to CH$_3$OH and HCOOH under UV/visible, Light, J. CO$_2$ Util. 18 (2017) 261–274.

[55] F.-L. Meng, H.-X. Zhong, Q. Zhang, K.-H. Liu, J.-M. Yan, Q. Jiang, Integrated Cu3N porous nanowire array electrode for high-performance supercapacitors, J. Mater. Chem. A 5 (2017) 18972–18976.

[56] P. Yang, L. Wang, H. Zhuzhang, R. Wang, M.-M. Titirici, X. Wang, Photocarving nitrogen vacancies in a polymeric carbon nitride for metal-free oxygen synthesis, Appl. Catal. B 256 (2019), 117794.

[57] P. Basu, Use of EPR spectroscopy in elucidating electronic structures of paramagnetic transition metal complexes, J. Chem. Educ. 78 (2001) 666.

[58] B.-w Sun, H.-y Yu, Y.-j Yang, H.-j Li, C.-y Zhai, D.-J. Qian, M. Chen, New complete assignment of X-ray powder diffraction patterns in graphitic carbon nitride using discrete fourier transform and direct experimental evidence, Phys. Chem. Chem. Phys. 19 (2017) 26072–26084.

[59] P. Niu, L. Zhang, G. Liu, H.M. Cheng, Graphene-like carbon nitride nanosheets for improved photocatalytic activities, Adv. Funct. Mater. 22 (2012) 4763–4770.

[60] S. Dias, K. Kumawat, S. Biswas, S.B. Krupanidhi, Solvothermal synthesis of Cu$_2$SnS$_3$ quantum dots and their application in near-infrared photodetectors, Inorg. Chem. 56 (2017) 2198–2203.

[61] J.-Y. Tang, X.Y. Kong, B.-J. Ng, Y.-H. Chew, A.R. Mohamed, S.-P. Chai, Midgap-state-mediated two-step photoexcitation in nitrogen defect-modified gC$_3$N$_4$ atomic layers for superior photocatalytic CO$_2$ reduction, Catal. Sci. Technol. 9 (2019) 2335–2343.

[62] Y. He, Q. Lei, C. Li, Y. Han, Z. Shi, S. Feng, Defect engineering of photocatalysts for solar-driven conversion of CO$_2$ into valuable fuels, Mater. Today 50 (2021) 358–384.

[63] Y. Liang, X. Wu, X. Liu, C. Li, S. Liu, Recovering solar fuels from photocatalytic CO$_2$ reduction over W^{6+}-incorporated crystalline g-C$_3$N$_4$ nanorods by synergetic modulation of active centers, Appl. Catal. B 304 (2022) 120978.

[64] J. Fu, K. Jiang, X. Qiu, J. Yu, M. Liu, Product selectivity of photocatalytic CO$_2$ reduction reactions, Mater. Today 32 (2020) 222–243.

[65] S. Gong, X. Teng, Y. Niu, X. Liu, M. Xu, C. Xu, L. Ji, Z. Chen, Construction of S-scheme 0D/2D heterostructures for enhanced visible-light-driven CO$_2$ reduction, Appl. Catal. B 298 (2021), 120521.

[66] Y. Li, B. Li, D. Zhang, L. Cheng, Q. Xiang, Crystalline carbon nitride supported copper single atoms for photocatalytic CO$_2$ reduction with nearly 100% CO selectivity, ACS nano 14 (2020) 10552–10561.

[67] T. Billo, F.Y. Fu, P. Raghunath, I. Shown, W.F. Chen, H.T. Lien, T.H. Shen, J.F. Lee, T.S. Chan, K.Y. Huang, Ni-nanocluster modified black TiO$_2$ with dual active sites for selective photocatalytic CO$_2$ reduction, Small 14 (2018) 1702928.